Environmental Processes (2024) 11:46
https://doi.org/10.1007/s40710-024-00721-7

RESEARCH

Cold Region River Flood Mapping and Scour Potential Prediction: Insights from Hydraulic Model Using Advanced Autonomous Surface Vehicles

Vida Atashi[1] **· Yeo Howe Lim**[1] **· Taufiq H. Mahmood**[2]

Received: 29 December 2023 / Accepted: 6 August 2024 / Published online: 28 August 2024

Abstract

This study aimed to map the 2022 flood with a 16.5-year return period near a bridge on the Red River, close to Grafton City, North Dakota, and evaluate the scour potential around the bridge. The Red River Basin (RRB) near Grand Forks, ND, and Emerson, ND, is a cold region river vulnerable to floods. Local scouring around bridge piers during floods can lead to hydraulic structure failure. An Autonomous Surface Vehicle (ASV) equipped with LiDAR DEM data from the ND DWR's LiDAR dataset was used to collect comprehensive bathymetry and discharge data, including the 2022 flood. The HEC-RAS model was used to create flood maps, and the Colorado State University (CSU) methodology was employed to assess local scour around the bridge pier. The study area recorded maximum velocities of 1.71 m/s, 1.87 m/s, and 1.56 m/s for discharge values of 368 m^3/s, 784 m^3/s, and 1335 m^3/s, respectively, with higher velocities recorded upstream of the bridge. The maximum water depth reached 13.14 m during the peak discharge of 1335 m^3/s. Higher discharge resulted in increased Froude number and contraction scour depth, with the latter continuing to increase even when the Froude number decreased as water reached the bridge deck. The study highlights the effectiveness of integrating ASVs, bathymetry, and LiDAR data to comprehensively understand flood dynamics and bridge scour in cold region rivers, offering the way for the development of effective flood control measures and strategies to safeguard critical infrastructure.

Highlights

- Flood mapping and bridge scour assessment was conducted using an ASV in the Red River.
- The integrated approach using bathymetry, LiDAR, and ADCP data enhanced accuracy.
- Higher discharge increased Froude number and contraction scour depth around the bridge.
- The study demonstrates ASV potential for efficient data collection in cold region rivers.
- The findings provide valuable insights for flood management and bridge scour mitigation.

Extended author information available on the last page of the article

Keywords Contraction scour depth · Flood mapping · HEC-RAS model · LiDAR data · Manning n-coefficient · Red River

1 Introduction

The rivers of the cold region plains with seasonally frozen condition are vulnerable to massive spring flooding due to lack of topography, frozen soil and basal ice presence during snowmelt period, thick snow accumulations, and river ice jams (Jeannotte et al. 2020; Neal et al. 2023). One of the most notable examples of such cold region rivers is the Red River (also known as Red River of the North), draining to Lake Winnipeg. Notably, the Red River segment and its adjacent floodplains, stretching from Grand Forks, ND, to Emerson, ND, are highly susceptible to recurring flood events indicated by a large area of prominent seasonal water area occurring during wet springs (Atashi et al. 2023). The region's low-lying topography and the formation of ice jams downstream in the Red River and Lake Winnipeg exacerbate flooding during wet spring seasons, as observed in 1997, 2009, 2011, and 2013. The frequent recurrence of flood incidents in this Red River segment underscores the importance of gaining a comprehensive understanding and proactively address flood risks in the region, aiming to minimize potential damage and protect the affected areas and communities (Atashi 2023; Rannie 2016; Schlauderaff 2021; St. George et al. 2022).

Despite the Red River of the North propensity for frequent flooding, there has been a notable scarcity of research specifically focused on flood forecasting in the region. The research by St. George et al. (2022) emphasizes the critical need for paleo flood investigations to better understand historical flood patterns, assess true flood risks, and inform flood protection infrastructure decisions for communities along the Red River of the North in Minnesota and North Dakota (St. George et al. 2022).

While existing studies have primarily centered on comparing the accuracy of various forecasting methods, ranging from classical statistical approaches to advanced machine learning and deep learning algorithms (Atashi et al. 2022), none have explored the potential benefits of incorporating bathymetry data into flood forecasting efforts in the Red River. This lack of research is particularly concerning given the recent findings of our spatial analysis of the Seasonal Water Area (SWA) and Permanent Water Area (PWA), which revealed a highly flood-prone section of the river near Grafton City, situated between Grand Forks and Emerson (Fig. 1c). Our recent study uncovered that this specific river segment consistently demonstrates a higher-than-average probability of experiencing severe flood events, emphasizing the critical need for targeted research to enhance our understanding of flood dynamics in this area (Atashi et al. 2023). To address this pressing research gap, our current study builds upon these preliminary results by focusing on this particularly susceptible region. By investigating the behavior of floods and the underlying causes of their heightened vulnerability in greater detail, we aim to develop more correct and reliable flood forecasting models that incorporate crucial bathymetry data. This comprehensive approach will not only advance our scientific knowledge of flood dynamics in the Red River but also offer valuable insights to support effective flood management and mitigation strategies in the region.

Moreover, cold region river bathymetry studies are rare due to weather-related challenges. In addition to weather-related obstacles, other challenges include extensive ice, limited accessibility to remote areas, safety concerns associated with extreme temperatures and

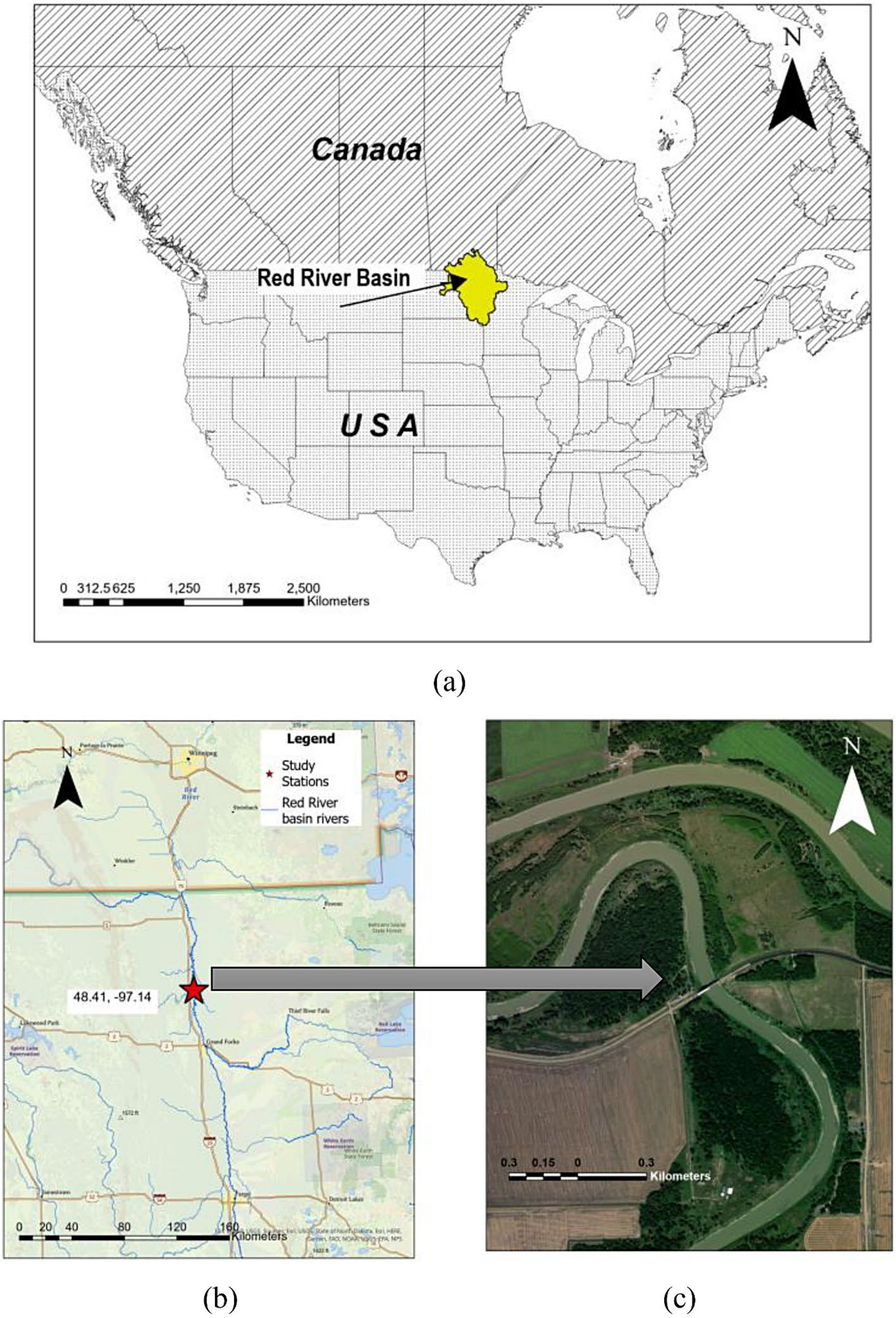

(a)

(b) (c)

Fig. 1 (**a**) Location of the research. (**b**) Red River of the North (**c**) Study section of the Red River East of Grafton, ND (48°24’47.56"N 97° 8’15.99” W) icy surfaces, limitations of sensors in icy water conditions, and difficulties in interpreting data due to the presence of ice and unique features. Due to the mentioned limitation, previous studies in cold regions have primarily relied on bathymetric maps such as SRTM data, TerraTec AS, and 5th generation (DTM 5G) bathymetric data georectified by the Norwegian Mapping Authority to verify the bathymetries (Armon et al. 2020; Bures et al. 2019; Flener et al. 2012; Salavitabar et al. 2022).

For instance, the study by Salavitabar et al. (2022) investigates underwater bathymetry mapping in Quebec's Nicolet River using WorldView-3 satellite images. It presents efficient approaches that eliminate the requirement for ground data calibration by concentrating on radiometric adjustments and water effects. These methods provide a reliable and cost-effective alternative to field surveys. Comparisons between before and after radiometric correction reveal considerable improvements (Salavitabar et al. 2022).

On a related note, our study stands out as the first to use in-field collected bathymetry data in the Red River of the North, resulting in a more accurate hydraulic model. While earlier research has offered valuable insights into the benefits of bathymetric data, they have not explored the potential advantages of directly collecting bathymetric data on-site. A notable aspect of this study is the use of the HYCAT system, which is innovative technology for data collection. In this research, we conducted flow measurements using both an ASV named HYCAT and an ADCP (Acoustic Doppler Current Profilers) which captures flow discharge, depth, and velocities. Additionally, a bathymetric survey of the streambed surrounding the bridge sites enabled the collection of water depth data in the form of point clouds for 3D bathymetric mapping and flood inundation analysis, using the HEC-RAS model (Brunner 2021). When paired with ADCP bathymetry data, high-resolution topographic data from LiDAR technology can be used to reveal intricate topographic features and improve the accuracy of inundation mapping. Combining bathymetry and LiDAR data can help create accurate flood maps, which will make it easier to create mitigation and prevention strategies to prevent flooding (Atashi 2023; Bialik et al. 2014; Muste et al. 2004; Salalila 2021).

In a similar vein, research by Vermeulen et al. (2014) explored a novel method for analyzing data from vessel-mounted ADCPs (Vermeulen et al. 2014) that deviates from the traditional assumption of equal flow between acoustic beams. It reduces the expected flow homogeneity and delivers more accurate velocity estimates, particularly in areas of high shear. It improves findings for complex surface flow investigations and has applications in sediment transport, flow division at bifurcations, and detailed flow patterns near obstructions or channel junctions. In another research (Khandelwal et al. 2023) the Navigator, a Lagrangian monitoring system, collects real-time data in surface freshwater ecosystems, offering insights into spatial and temporal variations. Equipped with water quality sensors and GPS, it finds changes linked to land use, wildfires, and recreational pond monitoring. Affordable and adaptable, it supports informed decision-making in hydrology and environmental management globally (Khandelwal et al. 2023).

Our research stands out as it encompasses bathymetry data collection over a significant distance in one of the intense flood years in Red River, 2022, which has not been extensively covered in existing cold region bathymetry studies. Particularly noteworthy is the novel approach of collecting data during a flood event, enabling the acquisition of precise and accurate information in real-time under challenging hydrological conditions. To the best of our knowledge, no research studies have specifically used an ASV like HYCAT as a moving boat for bathymetry purposes in flood-related research.

Due to the limitations of conventional methods, exact flood prediction in cold climates continues to be a significant issue, creating a vital gap in the field. For bathymetry (riverbed topography), satellite data is usually used instead of field data because of its higher accuracy and more detailed information. Large ice floes and heavy snowfall during the winter and spring melt seasons make gathering data more difficult and impede standard approaches. Moreover, the potential of high-quality bathymetry data for enhanced flood forecasting in cold climates has not yet been completely investigated in existing research, which has an impact on flood prediction and management techniques worldwide.

This research aims to address this global challenging gap by posing the following question: How can high-resolution, field-based bathymetry data collected during a flood event improve flood forecasting models in cold-region rivers? By directly addressing this question, this study explores the potential of using high-resolution, field-based bathymetry data, specifically gathered during a flood event, to enhance flood forecasting capabilities in cold regions. This approach offers a unique contribution to the international scientific community studying cold-region rivers: (1) Data collection during a flood event: This research stands out by collecting bathymetry data during a significant flood event (a 16.5-year flood in 2022) on the Red River. Collecting data in real-time under challenging hydrological conditions provides precise and accurate information, which has not been extensively covered in existing cold-region bathymetry studies. (2) High-resolution data over a significant distance: The study collected high-resolution bathymetry data over a 518-meter-long distance near the Grafton bridge (48°24’47.56"N 97° 8’15.99” W) during the flood event. This comprehensive data collection enables a detailed analysis of the river’s terrain and channel attributes. (3) Use of cutting-edge technology: The research employed the HYCAT, a multiparameter and portable survey Autonomous Surface Vehicle (ASV), engineered to provide surveyors with data access in remote regions that were previously challenging, costly, or inaccessible. This technology allows for efficient and accurate data collection even in difficult conditions. (4) Improving flood forecasting: By leveraging the collected bathymetry data, this research aims to provide valuable insights into the river’s terrain and channel attributes, which can be used to improve flood forecasting models in cold-region rivers.

The main goals of this research can be summarized as follows:

1. To perform a thorough mapping of the 2022 flood event near the Grafton bridge in the Red River of the North, a high-risk section of the Red River in the north during wet springs. This mapping uses bathymetric and LiDAR data and aims to capture the extent and characteristics of the flood event, providing valuable information about the spatial distribution of water levels and inundation patterns.
2. To assess local scour around the bridge pier and examine the erosive around the bridge pier using the established method developed by Colorado State University (CSU). The focus is to examine the erosive effects of the flow near the bridge pier during the 2022 flood event, providing insights into the potential scour depth and its spatial distribution.

2 Study Area

The Red River begins in Wahpeton, ND. The Otter Tail from Minnesota and the Bois de Sioux from South Dakota meet in Wahpeton to form the Red River of the North. It flows into Lake Winnipeg near the river's mouth, which is northeast of Winnipeg, Manitoba, Canada. Over its approximate 880-km length, the Red River of the North has varying slopes. The gradient of the Red River gradually decreases from an average of 0.00008 in the Fargo-Halstad region to 0.00002 in the Drayton-Pembina area. The Red River of the North is considered to have an exceptionally gradual slope, with a catchment area of 287,500 km^2 (Fig. 1a) (Babiracki 2015). Ice jams in the north generate significant flooding due to the frozen backwater effect (Lindenschmidt et al. 2012). When the river thaws in the spring, the warmer, southern portion melts first. The meltwater then moves north into colder temperatures, leaving the northern part of the RRB frozen and creating floods (Lim and Voeller 2009). Snowmelt processes are accelerated by rainfall in the spring and early summer, which coincides with remaining snow cover. The Red River Valley is more susceptible to flooding when the previously listed geographic factors are considered, especially in March and April. These elements emphasize the necessity of studying the dynamics of floods in this region allowing for a thorough investigation of the underlying causes that can have an impact on hydrological situation in springtime snowmelt floods.

A part of the Red River that leaves Grafton and flows east, Walsh County, North Dakota (48°24'47.56"N 97° 8'15.99"W) into Marshall County, Minnesota was chosen for this study (Fig. 1b). The study reach is approximately 18 km upstream of the Drayton United States Geological Survey (USGS) station, No. 05092000, North Dakota. This research area is between two USGS discharge data stations: The Red River at Drayton, ND (05092000) and the Red River at Grand Forks, ND (05082500), leaving around 18 km without discharge information. As mentioned previously, the region around Grand Forks, ND, and Emerson, ND, in the RRB's center region, experiences significant flooding during wet springs, leading to the occurrence of a noticeable seasonal water area (Atashi et al. 2023).

Concerns were also raised over possible scour holes close to the Red River of the North. The Grafton Bridge (5872 in Minnesota and 0017-140.372 in North Dakota), is a truss-supported, two-span bridge that spans Minnesota Trunk Highway 317 in Marshall County, Minnesota, and State Highway 17 in Walsh County, North Dakota. Given that bridge scour is the main factor contributing to bridge failure in the US, there are significant dangers involved (Richardson and Davis 2001). The research site spans a 518-meter-long section of the Red River at the specified location, approximately 300 m upstream and 200 m downstream of the bridge. We determined that this length was adequate to showcase the ASV's flood mapping capabilities, given that the ASV effectively navigated the entire study area and collected comprehensive data. The ASV-collected data was used to create a 3D flood model. The selected study area also offered sufficient size to capture the bridge's influence on the scour bridge formation process.

3 Materials and Methods

To create a visual representation of areas prone to flooding and analyze the scouring effects near bridge structures in HEC-RAS, we started by constructing a computational model of the waterway, using bathymetric measurements and LiDAR data as the foundational inputs. Next, we included other required parameters to the model including the roughness coefficient for the channel and overbanks based on earlier research. To compare anticipated water surface elevations, water depths, and water velocities with observed data, we ran the model. River cross-sections, sediment samples, flow discharges, pier shapes, and dimensions were the main sources of data used in this study. River length, research area maps, and Manning coefficient made up the secondary data. The model received all this data as input. In order to simulate the data, find the scour depth around the bridge piers, and create the flood map of the research region, we finally used HEC-RAS 6.0.0. Figure 2 presents a flowchart outlining our investigation, from data collection to modeling using HEC-RAS.

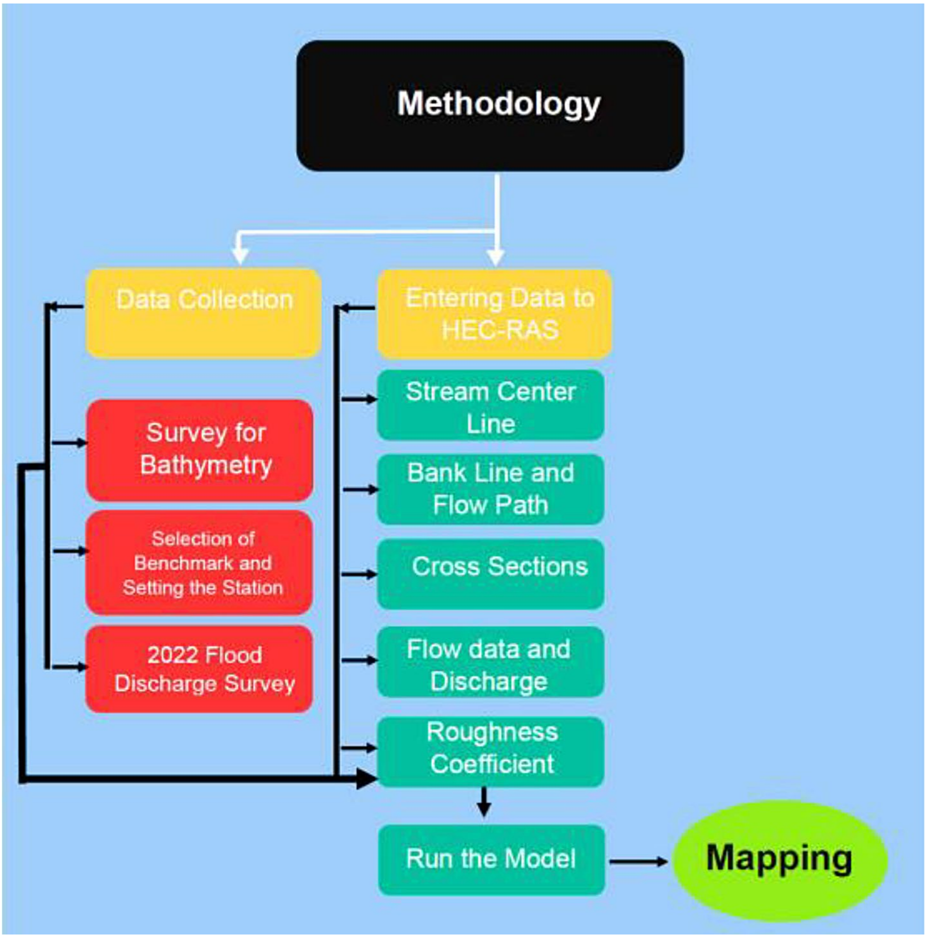

Fig. 2 Flowchart outlining the procedure from data collection through modeling using HEC-RAS

3.1 Bathymetry and LiDAR Data

The Red River's discharge, raw velocity, and bathymetry data were gathered using RiverSurveyor and HYPACK software, respectively. On the channel riverbed, the autonomous surface vehicle (ASV) known as HYCAT carried the stationary measurement instrument M9 ADCP (Fig. 3a), which was kept in place with the help of a remote controller (Fig. 3b). The HYCAT vehicle's versatile design enables it to navigate various water conditions, including shallow areas and tight spaces. Its autonomous operation facilitates continuous data collection, reducing the risk to human operators in hazardous flood environments. By integrating multiple sensors and transmitting real-time data, HYCAT enhances flood monitoring and emergency response, offering a cost-effective alternative to traditional methods. The M9 is capable of tracking discharge patterns, velocity speeds between 0 and 20 m/s, and water depths between 6 cm and 40 m (Carlson et al. 2019). Due to side-lobe interference, blanking distance, and draft, the ADCP is unable to measure the velocity in the upstream and downstream of the column of water. As a result, the discharge in these regions must be approximated using data gathered in the measured part of the water column. Therefore, the total of the draft, blanking distance, first and final depth cell locations, depth cell size, and side-lobe interference range finds an instrument's shallow-water limitation. This interference arises from weaker acoustic side lobes emitted alongside the main beam (Mueller et al. 2009). The energy reflected from the streambed in these side lobes can cause errors in Doppler shift measurements. The extent of interference varies, so careful consideration of the ADCP's beam pattern is essential for correct measurements. The percentage of the water column affected by this side-lobe interference ranges from 6% in a system with 20 degrees to 13% in a system with 30 degrees.

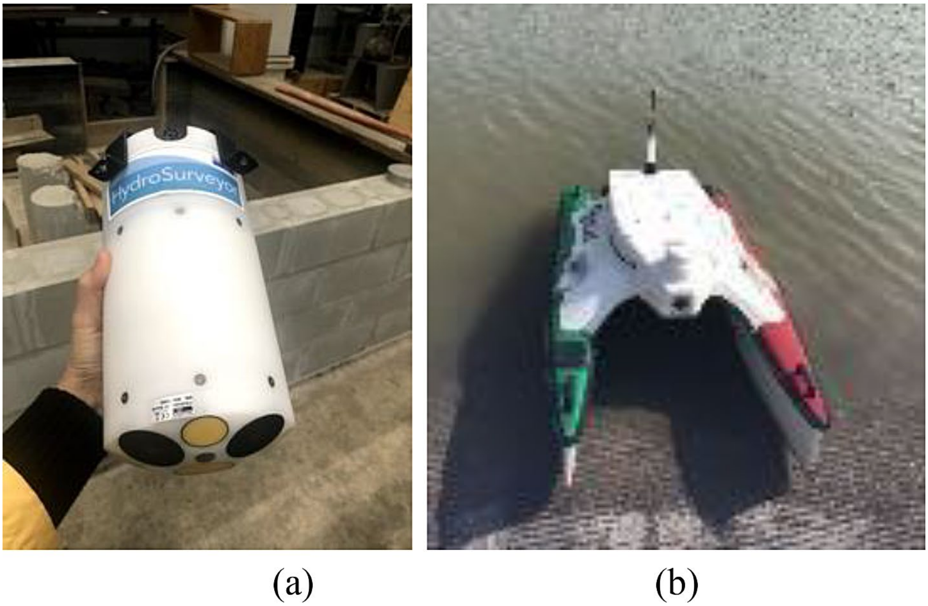

Fig. 3 (**a**) RiverSurveyor/HydroSurveyor M9 ADCP unit (**b**) ASV stationed at the Red River

Alterations in the river's morphology were quantified using an ADCP during the peak flow events that happened in April, May, and June of 2022. To initiate the compilation of bathymetric data, measurements were acquired by traversing the waterway perpendicularly to the direction of flow at designated transect locations, facilitated by a mobile vessel (Mueller et al. 2009; SonTek 2012). An average of 4.5 min were spent on each of the 64 transects that were conducted. Conversely, LiDAR data is commonly used for the generation of detailed topographic maps and digital elevation models. In our research, we acquired overbank elevation data from LiDAR scans provided by the ND DWR, featuring a resolution of 7.5×7.5 min. This dataset was instrumental in constructing cross-sections, serving as crucial input for flood mapping within HEC-RAS.

The discharge, which had a 16.5-year return time, was measured during the flood event that occurred in April and June of 2022. Using PeakFQ software that was obtained from the USGS, the return period was calculated (Veilleux et al. 2014). PeakFQ fits the Pearson Type III frequency distribution to the logarithms of instantaneous annually peak flows, following the guidelines specified by the USGS (Sando and McCarthy 2018). This ensures reliable flood-frequency analysis, accounting for various outliers and historical peaks (Flynn 2006). The dataset, which is based on peak discharge measurements gathered at the Grand Forks station, covers the years 1882 through 2021. Based on the probability of the flood happening and its frequency of occurrence, the return period is estimated. The return period is the average number of years between floods of a specific size or greater. In this research, the discharge varied from 375 m^3/s to 1335 m^3/s.

3.2 Model Description

The HEC-RAS 6.0.0 software was used in this study's hydraulic analysis, which performed a steady flow simulation to forecast the local scour depth surrounding an existing bridge. Manual inputs included sediment diameter (D_{50}) on each left and right overbank and channel. D_{50} measurements were obtained by collecting sediment samples from both sides of the riverbanks. Subsequently, these samples underwent thorough sieve tests in the soil mechanics laboratories to determine the particle size distribution. Furthermore, we used the HEC-RAS 6.0.0 software to create a 1D hydrodynamic model for accurately mapping flooding in the present Red River reach. To determine the local scour depth around an existing bridge, hydraulic analysis was carried out in this study utilizing the HEC-RAS 6.0.0 and a steady flow simulation.

The model employed the energy equation, the empirical Energy equation, to establish the relationship between friction energy loss, hydraulic resistance, river geometry, and river discharge. This subdivision of the flow to determine the total conveyance and velocity coefficient for a cross-section is based on the input cross-section n-value break points, which serve as the basis for partitioning the flow into both the overbank areas and the main channel using the HEC-RAS technique. The conveyance within each subdivision is determined using the expressed Manning equation (Chow 1959).

3.3 Processing Geometric and Hydrologic Data with the RAS-Mapper Tool

Both ADCP and LiDAR sources provided the bathymetry data needed to produce cross-sectional and hydraulic structural data for modeling. Once the geometric data was entered, the model construction process was completed by providing discharge and boundary conditions in a steady flow file. Steady flow data from six different discharges taken during the flood in 2022 were used for the HEC-RAS models. These steady flow data sets were crucial for simulating and analyzing the river's behavior under various flow conditions. The normal depth, which represents the uniform flow, was determined based on the slope of the study area.

The boundary conditions for both the upstream and downstream areas were set using the normal depth concept. To enhance bathymetry accuracy, along the 520-m study reach, we also examined twenty 30-m interval cross-sections and two 12-m interval cross-sections upstream and downstream of the bridge. HEC-RAS data was shown on maps and terrain models were created using RAS-Mapper. GIS data was extracted from overbank lines, centerlines, flow, and cross-section lines using river digitization which is shown in Fig. 4 (Banks et al. 2014). In Fig. 4, the solid lines in the centerline signify the flow path lines, while the numbered lines are cross-sections cut lines that were used to obtain terrain elevation data, contributing to the creation of a comprehensive ground profile spanning the channel flow. Channel overbanks are shown by the points at the end of cross-section lines; these points reflect the main channel overbanks for a given cross-section. Lastly, the research study area is shown by the dashed line.

3.4 Bridge Scour Modeling

The scour depth at bridge piers located on rivers can be determined by the software using hydraulic flow data, along with the shape and geometric characteristics of the bridge pier, and the composition and form of the riverbed substrate. The model for estimating the local scour depth around bridge piers in the software is known as the CSU model, which is described as follows (Ghaderi et al. 2019).

$$Y_s = 2.0\ K_1K_2K_3K_4\ \alpha^{0.65}Y_1^{0.35}Fr_1^{0.43} \tag{1}$$

where: Y_s = the maximum scour depth; α = width or diameter of the pier; Y_1 = the flow depth in the pier upstream; K_1 = the pier shape coefficient; K_2 = the coefficient of the impact angle;

Fig. 4 Plan view and reach details of the study

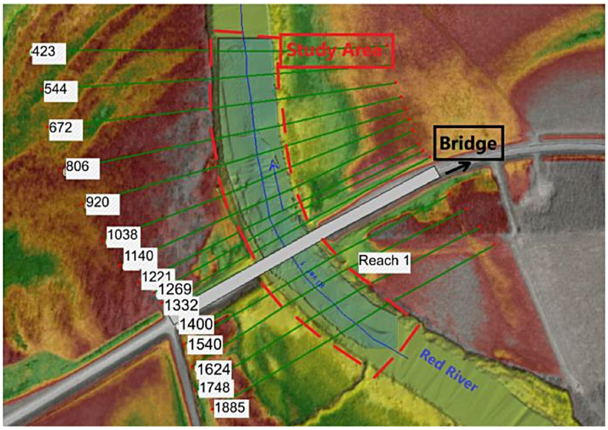

K_3=the bed condition coefficient; K_4=the bed's coefficient of reinforcement by the sediment particles; Fr_1= Froude number.

In the initial phase of the study, flood inundation mapping was generated utilizing the Ras-Mapper tool within HEC-RAS software, incorporating bathymetry and LiDAR data. HEC-RAS is widely recognized and employed by researchers for analyzing bridge scours (Ghaderi et al. 2019; Mehta and Yadav 2020; Namara et al. 2022; Noor et al. 2020; Pinos et al. 2019). In the second part, the research focused on mapping flood inundation using bathymetry and LiDAR datasets. This mapping provides crucial information for designing structures like rip rap to prevent scour by detailing the underwater topography.

4 Results

4.1 Model Coefficient

An observed flow of 368 m^3/s, 375 m^3/s, 411 m^3/s, 552 m^3/s, 784 m^3/s, 1026.5 m^3/s, and 1335 m^3/s at the river upstream was used from the flood event in 2022 with a 16.5-year return period. These flow rates are considered low, medium, and high flow in the Red River. In this study, we selected the value for Manning roughness coefficient based on previous studies which introduced ranges of Manning n-coefficient values for the Red River of the north, and we evaluated (Arcement and Schneider 1989). The selected n-coefficient value was then used in our hydrological analysis to improve the accuracy of flood prediction. Based on the literature review (Chow 1959; U.S. Army Corps of Engineers 2019), the initial value of the n-coefficient was set to be between 0.04 and 0.05 for the channel bed river and between 0.06 and 0.16 for the riverbanks.

Table 1 provides data on both observed and simulated water levels for different discharge values recorded during the 2022 flood event. To evaluate the simulation's accuracy, R-squared values were computed for the Red River bathymetry and simulated data. The R-squared statistic serves as a statistical indicator of how well the regression model aligns with the observed data, with higher values suggesting a stronger fit:

$$\begin{aligned} R^2 &= 1 - \frac{Sum\ Squared\ Regression\ (SSR)}{Total\ Sum\ of\ Squares\ (SST)} \\ &= 1 - \frac{\sum_0^N (y_i - \widehat{y_i})^2}{\sum_0^N (y_i - \bar{y})^2} \end{aligned} \tag{2}$$

Table 1 Manning's n-coefficient for observed and simulated water level data

Date	Q (m^3/s)	Water Elev. (m)	Water Elev. (Hec-RAS) (m)
		Observed Data	n_{channel}=0.046 n_{overbank}=0.06
4/8/2022	368	239.878	239.95
4/27/2022	1335	245.97	244.14
5/7/2022	1026.5	245.364	243.65
5/27/2022	784	243.54	243.25
6/12/2022	552	242.32	241.44
6/20/2022	411	241.1	240.20

The variable y_i is the i^{th} water level value generated by the model, while $\widehat{y_i}$ denotes the i^{th} water level value obtained from measured data. The mean water level value of the measured data series is shown by $\bar{y_i}$, and N signifies the total number of data series.

Given that the simulated and observed water surface profiles closely match, the best Manning n-coefficient values to utilize are 0.046 for the river channel and 0.06 for the overbanks, according to the 93% coefficient of determination (R^2) value. The value of Manning n-coefficient for the main channel is displayed by $n_{Channel}$, and the value for the overbanks is shown by *n_overbank*. Since the vegetation in the study section is comparable in the left overbank (*LOB*) and right overbank (*ROB*) sections, only one value is used for both overbanks.

4.2 Model Flood Mapping

A national framework has been set up through National Oceanic and Atmospheric Administration (NOAA) and *USGS* collaboration to consistently integrate bathymetric and LiDAR topographic data into seamless digital elevation models for U.S. River areas. This framework leverages ADCP's versatility to incorporate multi-source data and uses Ras Mapper software to combine datasets into continuous, tiled terrain surfaces with uniform resolution and seamless edges between tiles. It provides standards for producing integrated DEMs of river areas by harmonizing contributions across stakeholders.

Figure 5 illustrates the topographical surface, encompassing numerous cross-sections within the HEC-RAS model for the study area near the Grafton Bridge along the Red River. The simulated inflow discharge water surface profile of 368 m^3/s and 1335 m^3/s are depicted in Fig. 5a and b, respectively, which are the low and high flow values of the measured data during the research period, respectively.

a) The ground elevation profile (dark line) shows a more pronounced V-shaped channel which is the main channel, with steeper bank slopes on both sides. The dark line represents the ground elevation profile across the cross-section. It shows a relatively flat and shallow channel bed, with slightly higher elevations towards the outer edges, likely representing the channel banks or natural berms. Station values, which are shown at the end of each cross section are essentially the distance along the cross-section line. The numbers on this axis range from 133 to 1691, showing a cross-section width of

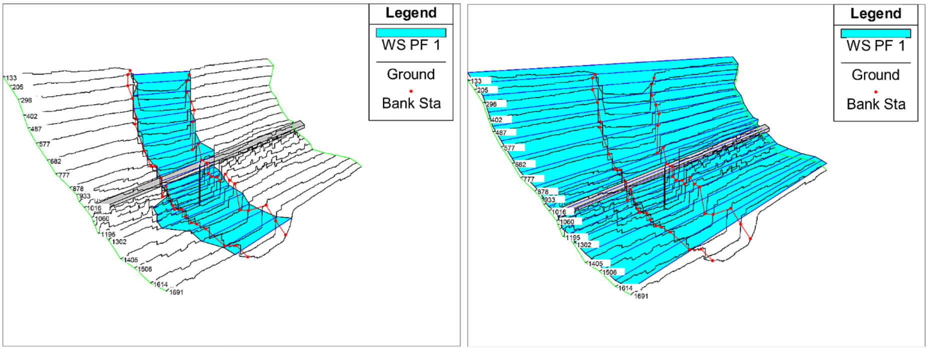

(a) (b)

Fig. 5 HEC-RAS simulated topographical surface profile for (**a**) Q = 368 m^3/s, and (**b**) Q = 1335 m^3/s

approximately 1558 units. The area labeled "WS PF 1" is the calculated water surface elevation for a specific flow event or profile. In this case, the water surface elevation remains well below the ground elevation across the entire cross-section, indicating that the flow is contained within the main channel and does not overtop the banks. The dots connected with lines indicate the locations of the left and right bank stations, which are typically used to define the main channel boundaries for hydraulic calculations.

b) In contrast, this cross-section is a deeper channel section with its floodplain area. The water surface area for the same flow event ("WS PF 1") is significantly higher relative to the ground elevation, especially in the center of the channel showing that the flow is potentially exceeding the channel's capacity, increasing the risk of overbank flooding or overtopping of the banks. The bank stations (dotted line) are located much closer to the center of the channel, reflecting the narrower channel width at this location. The entire overbank was under water during April 2022 with Q = 1335 m^3/s flood near Grafton (Fig. 5b).

It should be noted that due to the left overbank's lower elevation and incorporation of the "backwater phenomenon", the river flow reached the overbanks on the left overbank first. According to Charbeneau and Holley (2001), the term "backwater" describes the rise in water level that occurs when the bridge piers obstruct the flow and raises water levels upstream for subcritical flows (Charbeneau and Holley 2001).

Figure 6 highlights the surface water levels at two key cross-sections within the study area: cross-section No. 1885 (the first cross-section) and cross-section No. 423 (the last cross-section), as depicted in Fig. 4. These levels were extracted from Digital Elevation Models (DEMs) using geometry data. The horizontal axis, representing the width of the cross-section, spans a range of approximately 500 m, indicating a relatively wide cross-section. The vertical axis represents elevation in m. The study of the two cross-sections allows for an analysis of the following information: The primary channel width for Cross-Section No. 1885 is roughly 138 m, measured between the left and right bank stations. The total width of the floodplain and overbank sections on either side of the main channel is approximately 488 m. Cross-Section No. 423, on the other hand, displays a distinct profile. In comparison to Cross-Section No. 1691, the cross-section's horizontal axis covers a considerably smaller range, suggesting a narrower cross-section width overall. The main channel's width—the distance between the left and right bank stations—is roughly 98 m. This is a considerable reduction from the 138 m shown in Cross-Section No. 1885.

The simulation findings reveal that cross-section No. 423, positioned as the final designed cross-section, experiences lesser flood impact compared to cross-section No. 1885, which is upstream of the bridge. This susceptibility to flooding is seen particularly at a discharge

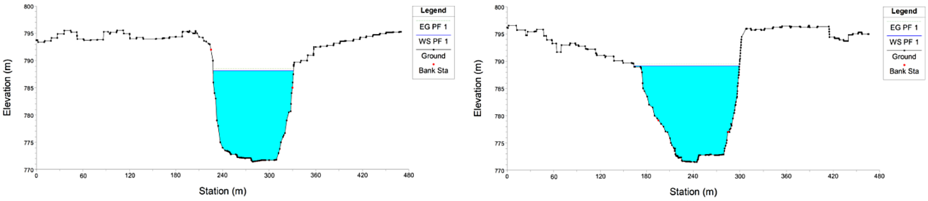

(a) (b)

Fig. 6 Water depths at the upstream and downstream cross-sections (**a**) Cross-section No. 1885. (**b**) Cross-section No. 423

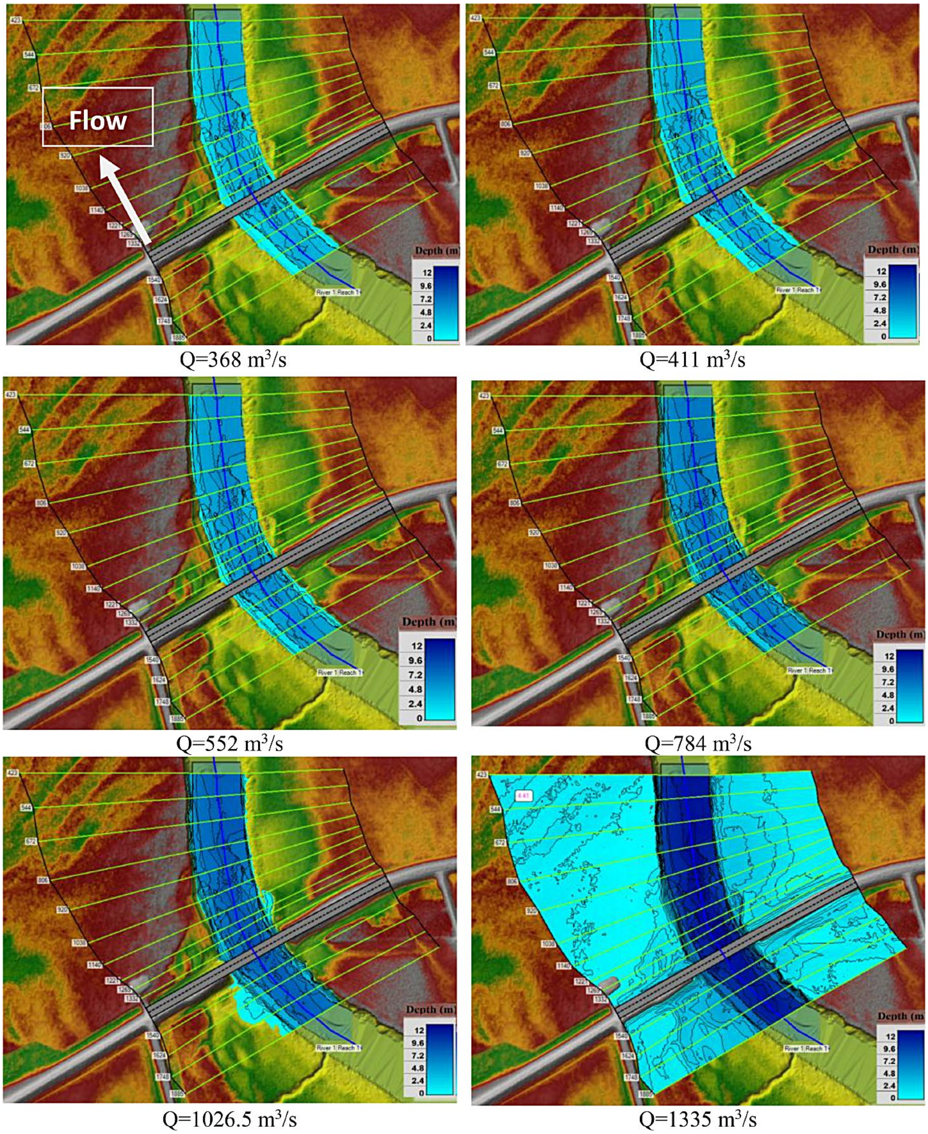

Q=368 m^3/s

Q=411 m^3/s

Q=552 m^3/s

Q=784 m^3/s

Q=1026.5 m^3/s

Q=1335 m^3/s

Fig. 7 Simulated flood inundation map of Red River near Grafton from April 2022 to June 2022 flood event for different discharges (base map from Google Earth (Pro 08/10/2015))

of Q = 784 m^3/s, as illustrated in Fig. 6a, b. The mean water level for Q = 784 m^3/s at cross-sections No. 423 and No. 1885 is 238.48 m (about 782.41 ft) and 238.95 m (about 783.96 ft), respectively, which shows a drop of 0.47 m in water elevation between upstream and downstream. The existence of bridge piers as an abutment in the streams will affect the flow and riverbed locally, causing the water to flow faster, the bridge to scour, potentially jeopardizing the structure. A faster cross-section would have less depth when the discharge is the same, according to the continuity equation.

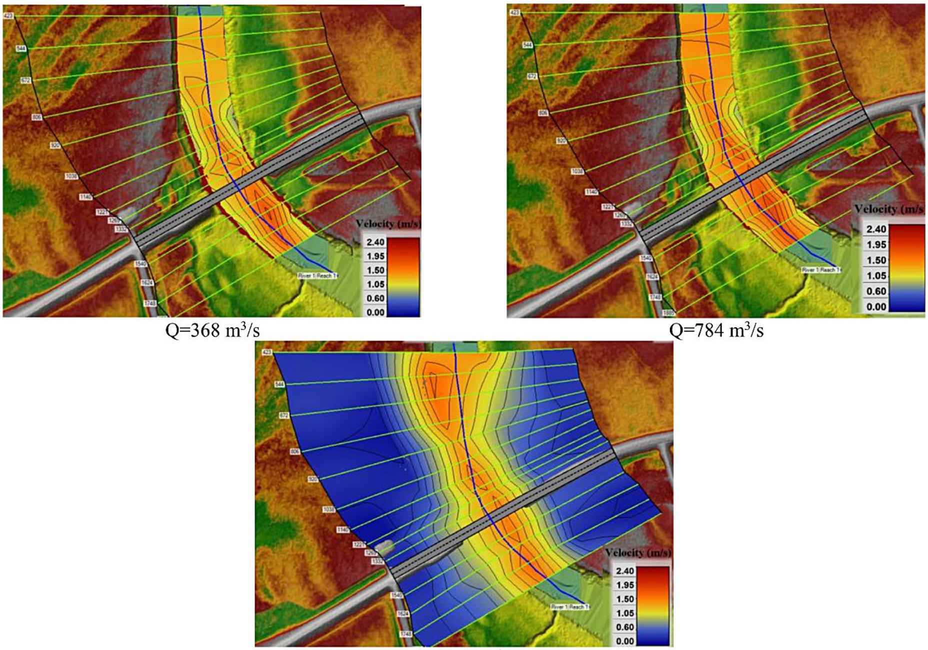

Q=368 m^3/s

Q=784 m^3/s

Q=1335 m^3/s

Fig. 8 Simulated velocity distribution for Q = 368 m^3/s, 552 m^3/s, and 1335 m^3/s (base map from Google Earth (Pro 08/10/2015))

Figure 7 presents the flood map, illustrating depth variations at each cross-section during a steady flow simulation. The simulated flood maps clearly display changes in water depths along the channel, with color used to highlight these differences. Six discharges were recorded over six time periods, from April 2022 to June 2022. The peak flow occurred on April 27th at the study section, with a discharge of Q = 1335 m^3/s. During this period, the discharges ranged from 368 m^3/s to 1335 m^3/s.

The flood inundation maps show the extent of flooding for different discharge values ranging from 368 m^3/s to 1335 m^3/s. As the discharge increases, the inundated area expands, indicating a larger area affected by floodwaters. At the lowest discharge of 368 m^3/s (top left image), the flooding is mostly contained within the main river channel, with minimal overbank flooding. As the discharge increases to 411 m^3/s (top right image), the inundation area begins to expand, with areas outside the main channel becoming flooded. At 552 m^3/s (bottom left image), the flooding becomes more extensive, with larger areas of overbank inundation along the river's floodplain. The image for 784 m^3/s (bottom right image) shows a significant increase in the flooded area, with a substantial portion of the floodplain and surrounding areas becoming inundated. The highest discharge of 1026.5 m^3/s (middle left image) and 1335 m^3/s (middle right image) represent the most severe flooding scenarios, with widespread inundation across the floodplain and surrounding areas.

Downstream cross-sections, located beyond the bridge, exhibited shallower depths during peak discharge time, while the upstream cross-sections were more profoundly impacted by the flood. The water level tends to be higher upstream of a bridge due to the pier acting as an obstacle, causing the water to funnel through a narrower passage. This constriction

Date	Q(m^3/s)	Cross section
4/8/2022	368	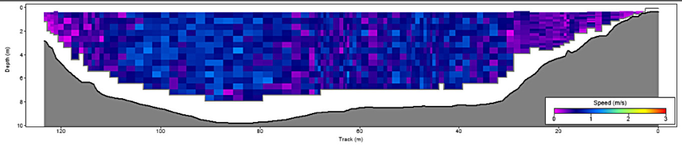
4/28/2022	1335	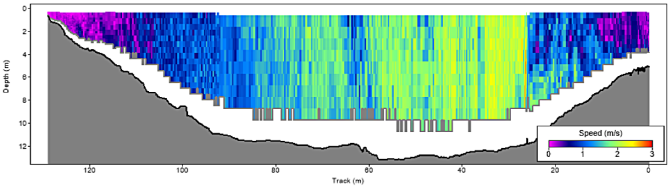
5/7/2022	1026.5	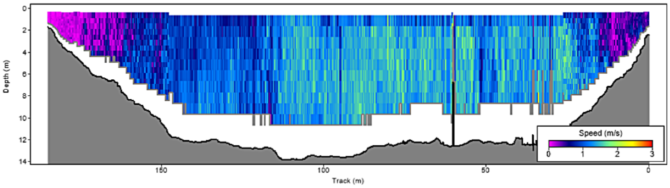
5/27/2022	784	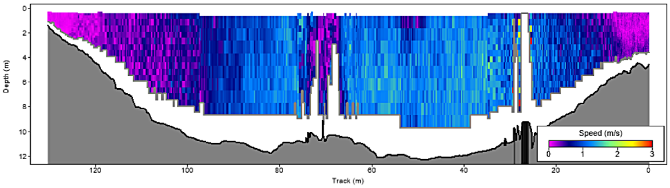
6/12/2022	552	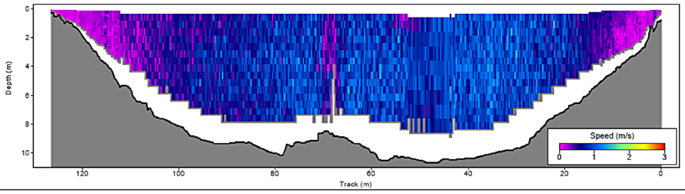

Fig. 9 Velocity spatial distribution on cross section after the bridge measured using an ADCP

leads to water accumulation and elevation around the bridge. Because of the Red River's particularly flat terrain, the HEC-RAS model's estimate of the flood inundation extent varied noticeably in response to slight changes in water depth.

It is worth highlighting that the middle section of the river showed deeper flow, particularly towards the end of the section. Given this observation, it may be prudent to assess the necessity for proper protective measures to mitigate potential risks associated with increased depth in that region. As the flow progresses towards the end of the study section, it meets another curve, with the outer bend situated on the right side. This configuration causes water to deepen on the outer bend while becoming shallower than the centerline on the inner side. The interplay between the flow and the outer bend contributes to these variations in depth, further influencing the river's hydrodynamics.

Figure 8 displays the velocity distribution results for three different discharge scenarios: 368 m^3/s, Q = 784 m^3/s, and 1335 m^3/s. These velocity mapping effects play a crucial role in reducing erosion along the river overbanks and around the bridge piers. An analysis of the outcomes from the 2022 flood event across all three discharge scenarios reveals a consistent observation.

Before the bridge on the right side, the inner bank shows a convex shape, creating a larger curve. This increases the cross-sectional area, leading to a decrease in flow velocity based on the principle of continuity. The water velocity is higher on the left side (outer bend) before the bridge. After passing the bridge, the flow shifts towards the left side due to interaction with the bridge piers, acting as hydraulic obstacles. This redirection concentrates flow towards the left side, resulting in higher velocity after the bridge on the left side (outside of the bend) (Fig. 4).

The fast counter lines indicate the presence of eddy flow, primarily influenced by the bridge piers. These circular currents significantly impact downstream flow patterns and water velocities. Recognizing and accounting for these flow dynamics becomes crucial in the design and construction of bridges, as they can influence the hydraulic forces exerted on the structure and the potential for erosion in surrounding areas. With increasing discharge values, the intensity of fast-moving eddy flow becomes more pronounced after the bridge pier, potentially leading to increased scouring. In the river bend, eddy flow directs the velocity vectors towards the outer surface of the bend and the inner bed, affecting overall flow dynamics. Consequently, protective measures are necessary on this side of the river overbank to prevent erosion.

In the specific case of our study, when the discharge reaches 784 m^3/s, it stands for a critical point where the channel experiences its maximum velocity. This occurs due to the substantial volume of water flowing through the channel, maximizing its capacity. However, once the discharge exceeds this threshold, such as at $Q = 1335$ m^3/s, several factors come into play that contribute to a reduction in velocity. The increased flow rate intensifies frictional losses, as the water exerts greater force against the channel walls, resulting in higher friction and energy dissipation. Consequently, the overall velocity diminishes compared to the earlier discharge, showing a decrease in flow efficiency.

Moreover, it is essential to consider the channel's capacity limitations. If the dimensions of the channel, such as its width or depth, are not designed to manage extremely high flow rates, it can lead to flow disturbances, turbulence, and a later decline in velocity. These limitations in channel capacity restrict the flow and prevent it from keeping the same high velocity seen at lower discharge rates in our specific case.

Figure 9 depicts the velocity and bathymetry observations obtained using ADCP during the flood event in 2022 in the Grafton section of the Red River. Specifically, the cross-section displayed corresponds to an immediate location after a bridge pier. Within the data, a strip of zero velocity is noticeable, attributed to the presence of the bridge pier. Notably, in certain cross-sections, this strip may be absent, showing that the ADCP location mounted on HYCAT is slightly displaced from the immediate vicinity of the bridge. This deviation can be attributed to wind-induced drift or high velocity, causing HYCAT to traverse a few feet further downstream, thus collecting data for a cross-section slightly downstream of the bridge.

The velocity range observed spans from 0.0 to 2.44 m/s, with zero velocities evident at both riverbanks and maximum velocities occurring on the right side of the bridge pier (from upstream to downstream). This higher velocity is attributable to the morphology of the river in the study section. More specifically, a sharp bend in the river induces a tendency for the stream flow lines to gravitate towards the outer bank, resulting in the occurrence of maximum velocities at that location (Nezaratian et al. 2023).

In general, as water approaches the upstream side of the bridge pier, the velocity intensifies due to flow area constriction induced by the presence of the pier. This constriction accelerates the flow, leading to higher velocities in proximity to the pier. Subsequently, as the water circumnavigates the pier, it enters a transition zone characterized by a gradual decrease in velocity. This deceleration can be attributed to the expansion of the flow area downstream of the pier. As the flow redistributes itself and adjusts to the wider channel, velocities diminish within this downstream face region. Regarding the maximum observed velocity, the highest flow collected on April 28th exhibited a velocity of 2.15 m/s. In contrast, velocities of 0.82 m/s and 1.06 m/s were recorded for flow discharges of 368 m^3/s and 552 m^3/s, respectively.

Figure 10 illustrates measured discharges during the 2022 flood event at our study site and the USGS data for Grand Forks, found approximately 65 km (about 40.39 mi) upstream. Round points stand for our field measurements, while the square point hydrograph depicts Grand Forks' data. Spanning from April 1st to June 30th, our field data aligns with USGS records at Grand Forks, particularly in low discharges, showing a reliable correlation. Peak discharge values also logically correspond with the upstream location of Grand Forks, underscoring the minor influence of tributaries like Turtle River on the Red River's discharge. This alignment supports the validity of our measurements in reflecting upstream conditions at Grand Forks.

Furthermore, to accurately capture the flow characteristics of the Red River, Fig. 10 additionally incorporates mean daily values from the Drayton USGS station shown by triangle points. This inclusion, considering the approximate 6-day travel time for peak flow between Grand Forks and Drayton, provides a more holistic understanding of the flow dynamics.

As mentioned earlier, the study area is located close to the Drayton gauge. On April 28, 2022, the study reported a measured Q of 1335 m^3/s. For comparison, Grand Forks' mean published Q is 1693 m^3/s and Drayton's is 1408 m^3/s. Integrating these additional data

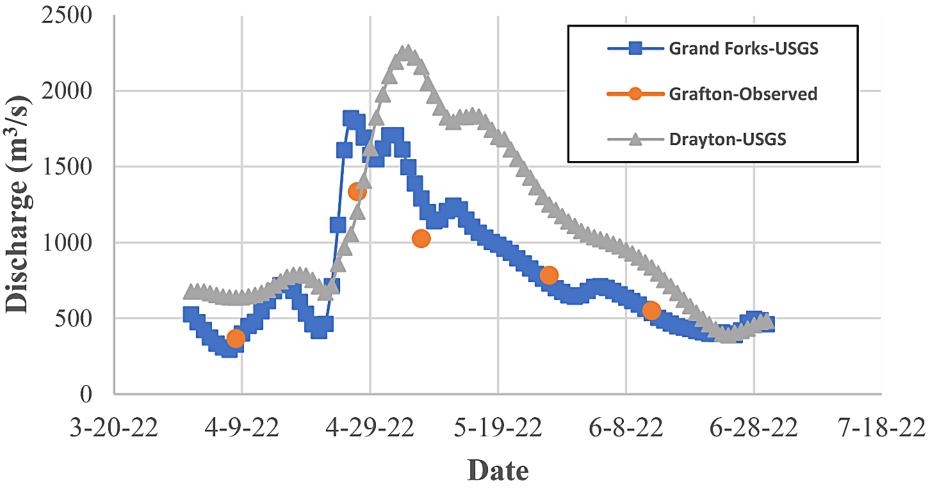

Fig. 10 Comparison of observed (Grafton) and USGS (Grand Forks) discharges during the 2022 Flood

points corroborates the validity of our measurements and supports our conclusions on the travel time of peak flows.

4.3 Model Scour Bridge

This study predicted local scours at a bridge using HEC-RAS 6.0.0. The software automated most calculations for contraction scour but needed manual input for sediment size. HEC-RAS calculated the critical shear velocity and applied the CSU equation to estimate scour depth near the piers, visualized in Fig. 11.

Figure 11 depicts the relationship between contraction scour depth (Y_s) and the Froude number (F_r) for the existing bridge as discharge increases. When the discharge rises from Q=552 m³/s to Q=1026.5 m³/s, there is a marked increase in the Froude number. Further, between Q=368 m³/s and Q=411 m³/s, as the water level surpasses the bridge deck, both the contraction scour depth and Froude number rise. However, at a discharge of 1335 m³/s, the water level reaches the bridge deck, resulting in a deeper contraction scour depth while the Froude number decreases.

Higher discharge increases velocity and the Froude number due to greater inertial forces. However, near the bridge deck, the reduced water depth shifts control to gravity, which lowers the Froude number despite the high velocity. As water approaches a bridge, the channel narrows because of the bridge piers or abutments. This constriction accelerates the water as it flows through the bridge opening, reducing the water depth. The focused flow around the piers or abutments heightens the risk of erosion and scour at the bridge foundations. Although the Froude number decreases, the contraction scour depth continues to grow because the high-water velocity erodes the riverbed, leading to deeper contraction scour.

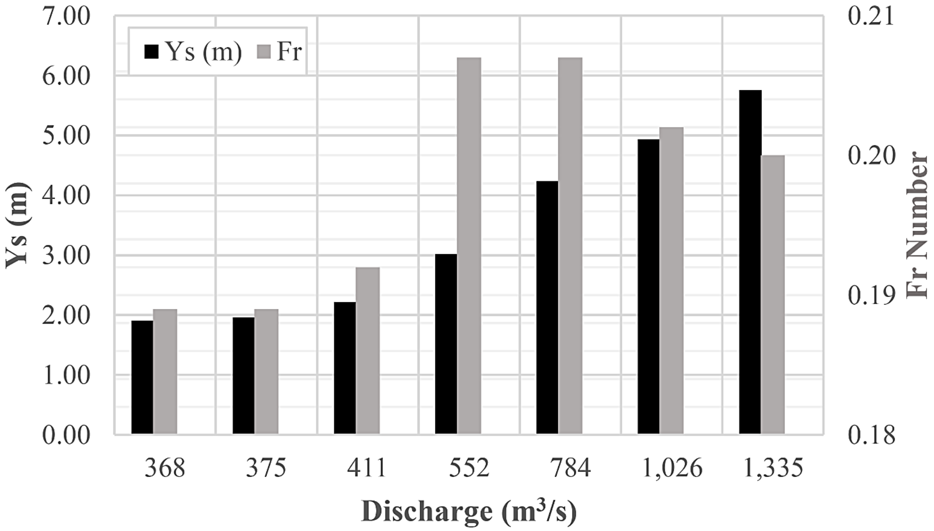

Fig. 11 Discharge vs. Froude number and contraction scour depth

5 Discussion

Our study stands out by utilizing ADCP data for bathymetry and discharge information, enabling a more precise flood map and finding high potential scour regions. To date, our study is one of the very few applications of ADCP data in the Red River. We employed an Autonomous Surface Vehicle (ASV) to gather bathymetry and discharge data under various flow conditions, which greatly contributes to the authenticity and accuracy of our findings for future flood event prognostications. In addition, our study also focuses on riverbed scour phenomena occurring around the bridge piers. While many studies have explored scour models, very few have simultaneously examined the potential benefits of high-resolution bathymetry data in both flood mapping and bridge scour assessment. The CSU model used in this study for estimating local scour depth around bridge piers is well-established and widely used, and its application with bathymetry data in this specific region is novel. The study area covered about 300 m upstream and 200 m downstream of the bridge, which provided enough data for creating a 3D model of the flood and evaluating the potential scour depth and spatial distribution.

Our research addresses a significant gap in flood forecasting and scour modeling specifically focused on the Red River near Grand Forks and Emerson, ND, which is a highly susceptible section to severe floods. One aspect that sets our study apart from earlier research efforts is the use of bathymetry data collected over a considerable distance during an intense flood year in the Red River. Most existing flood forecasting and scour modeling studies in the region have primarily relied on satellite data, which may have limitations in accuracy and reliability, especially in cold regions. By incorporating cutting-edge technology, such as the HYCAT Autonomous Surface Vehicle (ASV), for bathymetry data collection, we overcame weather-related challenges and achieved real-time data acquisition under challenging hydrological conditions. Previous studies have mostly centered on flood mapping and scour assessment using singular methods like Lidar data or modeling. In contrast, our approach innovatively combines both Lidar data and HEC-RAS modeling, providing a more comprehensive and exact perspective. Additionally, we introduce HYCAT, a novel device, further enhancing the uniqueness of our method and potentially yielding advanced flood mapping and scour assessment insights. We found that combining approaches, such as HEC-RAS and HEC-GeoRAS for flood extent, and LiDAR DEM for scour depth, provides a more accurate understanding of flood risks. Integrating diverse methods enhances flood risk assessment for better mitigation strategies (Mehta and Yadav 2020; Namara et al. 2022; Pathan and Agnihotri 2021; Pinos et al. 2019; Silvia et al. 2021; Zheng et al. 2018).

The flood inundation mapping revealed that the maximum water depth reached 13.14 m during the peak discharge of 1335 m^3/s. We also seen depths of 9.54 m and 10.61 m at discharges of 368 m^3/s and 784 m^3/s, respectively. The velocity distribution showed that the highest recorded velocities were 2.15 m/s, 1.87 m/s, and 1.56 m/s for the respective discharges mentioned above. Notably, we found that the velocity was higher on the right side of the river, indicating the influence of the outer bank and the presence of eddy flows around the bridge piers. Our study area was about 18 km upstream of the Drayton *USGS* station, and the Red River has a gentle slope with a catchment area of 287,500 km^2.

The results of bridge scour modeling proved that there was an increase in the contraction scour depth with increasing discharge, reaching a maximum of 2.44 m for the discharge of 1335 m^3/s. Additionally, the Froude number increased with higher discharges, indicating greater inertial forces. However, when the water level rose to the bridge deck, the Froude number decreased, whereas the contraction scour depth kept increasing due to the persistent high-water velocity around the bridge piers.

As a further illustration, Fig. 12 offers a thorough examination of the river's profile with a discharge of Q = 784.38 m³/s. The carefully crafted legend and magnification improve visibility and understanding of the depth and speed changes. The perception of the characteristics and dynamics of the river in respect to the given discharge is greatly enhanced by this visualization. The maximum recorded velocities in the study area were 1.71 m/s, 1.87 m/s, and 1.56 m/s for discharge values of 368 m³/s, 784 m³/s, and 1335 m³/s, respectively. These velocities were observed occurring before the bridge (Fig. 4), highlighting the significance of the bridge and its impact on the flow characteristics of the river.

6 Conclusions

This research addresses two areas concerning the Red River: the mapping of the 2022 flood on a vulnerable area near a bridge in proximity to Grafton City, North Dakota, and the evaluation of scour potential encompassing the bridge piers. The employment of an Autonomous Surface Vehicle (ASV), coupled with LiDAR DEM data sourced from the ND DWR's LiDAR, facilitated a comprehensive gathering of bathymetry and discharge data

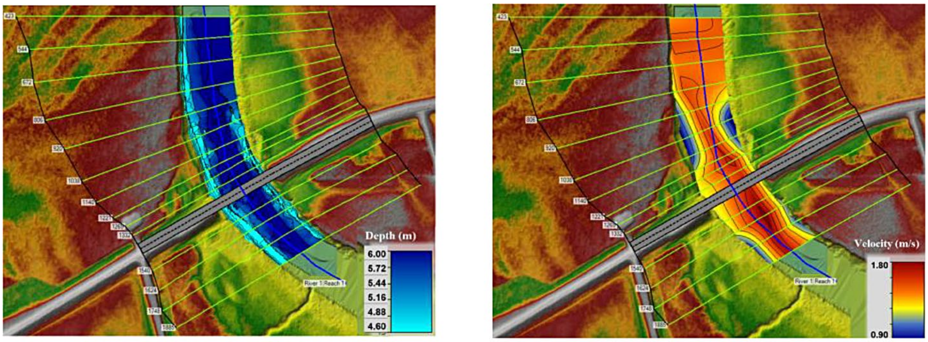

Depth Velocity

Q=1026.5 m³/s

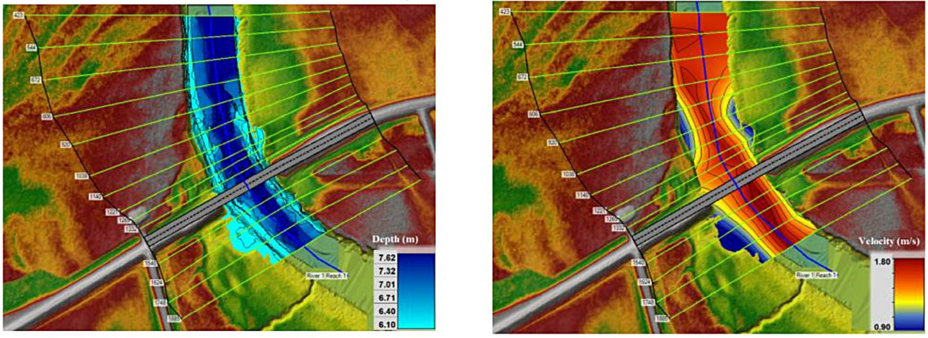

Depth Velocity

Q=784 m³/s

Fig. 12 River Profile Visualization at Q = 1026.5 m³/s and Q = 784 m³/s: Depth and velocity Variations across diverse flow conditions. This combined approach not only reveals detailed riverbed features and water flow patterns but is also significant for two main reasons:

Firstly, the Red River Basin (RRB) near Grand Forks, ND, and Emerson, ND, is a notable case of a cold region river vulnerable to floods. Frequent flooding, highlighted by a large seasonal water area during wet springs, emphasizes the need for improved flood comprehension. Second, this research marks the first utilization of an ASV to gather data in one of the unique cold region rivers, fraught with seasonal freezing challenges. This breakthrough approach enhances our ability to comprehensively study and manage hydrological phenomena in regions characterized by dynamic climatic conditions. The results can be outlined as follows:

1. This research seeks to identify the optimal Manning coefficient to enhance flood prediction accuracy for the Red River. By analyzing previous studies and conducting statistical assessments, the study found that a coefficient of determination (R^2) of 93% was achieved. The ideal Manning n-coefficient values determined were 0.046 for the river channel and 0.06 for the overbanks.
2. Bathymetric data were obtained using a combination of ADCP, ASV, and LiDAR technologies to analyze the flow during a 2022 flood event. The HEC-RAS model was utilized to create flood maps, which revealed an eddy flow developing just after the bridge, growing larger as flow discharge and velocity increased. The consistency between different methods underscored the effectiveness of integrating ADCPs with ASV and LiDAR data for flood inundation mapping, thanks to the comprehensive data on bathymetry, flow velocity, and discharge.
3. Additionally, the study demonstrated that as discharge increases, both the Froude number and contraction scour depth rise. However, once the water level reached the bridge deck, the Froude number decreased while the contraction scour depth continued to grow due to the high velocity. The presence of bridge piers, which narrow the channel, was found to focus the flow and elevate the potential for scour.

The research offers valuable insights into flood mapping and scour assessment within the context of the Red River. Nonetheless, it is essential to acknowledge inherent limitations. The reliance on specific data sources, such as LiDAR DEM data, could potentially impede the methodology's broader applicability in regions lacking access to these resources. Moreover, the sensitivity of results to model parameters introduces an element of uncertainty. Despite these constraints, the integrated approach shows improved accuracy in flood mapping and assessment of scour potential. This study's implications reverberate in the call for accessible and reliable data sources while highlighting the need to consider parameter sensitivity for precise flood management applications.

Acknowledgements We would like to thank The North Dakota Department of Transportation (NDDOT) for their financial support.

Author Contributions VA and YHL were responsible for conceptualization of project. VA and YHL developed methodologies for sampling and data analysis. YHL supervised the design of experiments with assistance from VA. VA and YHL contributed towards acquisition of data. VA led efforts to organize, analyze, and interpret data. VA, YHL, and THM were responsible for data validation. YHL and THM served as supervisors on the project. YHL and THM led efforts to acquire and administer research funds. VA drafted the original manuscript and all authors reviewed and assisted with editing the manuscript.

Funding This research was funded by the North Dakota Department of Transportation, grant number UND0026475. HYCAT used in this study can be purchased online at https://www.ysi.com/hycat, and ADCP MP used in this study can be purchased online at https://www.ysi.com/sontek-m9.

Data Availability No datasets were generated or analysed during the current study.

Declarations

Conflict of Interest The authors declare no conflict of interest. The funders had no role in the study's design, the collection, analyses, or interpretation of data, the writing of the manuscript, or the decision to publish the results.

References

Arcement GJ, Schneider VR (1989) Guide for selecting Manning's roughness coefficients for natural channels and flood plains. US Government Printing Office, Washington, DC. https://doi.org/10.3133/wsp2339

Armon M, Dente E, Shmilovitz Y et al (2020) Determining bathymetry of shallow and ephemeral desert lakes using satellite imagery and altimetry. Geophys Res Lett 47(7). https://doi.org/10.1029/2020GL087367. e2020GL087367

Atashi V (2023) Dynamics of Flood Flow in Red River Basin. Dissertation, University of North Dakota

Atashi V, Gorji HT, Shahabi SM et al (2022) Water Level forecasting using Deep Learning Time-Series Analysis: a case study of Red River of the North. Water 14(12):1971. https://doi.org/10.3390/w14121971

Atashi V, Mahmood TH, Rasouli K (2023) Impacts of climatic variability on surface water area observed by remotely sensed imageries in the Red River Basin. Geocarto Int 2023:1–18. https://doi.org/10.1080/10106049.2023.2209541

Babiracki D (2015) Lateral Migration of the Red River, in the Vicinity of Grand Forks, North Dakota. Undergraduate Thesis, University of North Dakota. https://commons.und.edu/senior-projects/114

Banks JC, Camp JV, Abkowitz MD (2014) Adaptation planning for floods: a review of available tools. Nat Hazards 70(2):1327–1337. https://doi.org/10.1007/s11069-013-0876-7

Bialik RJ, Karpiński M, Rajwa A (2014) Discharge measurements in lowland rivers: field comparison between an electromagnetic open channel flow meter (EOCFM) and an acoustic Doppler current profiler (ADCP). In: Achievements, History and Challenges in Geophysics: 60th Anniversary of the Institute of Geophysics, Polish Academy of Sciences, pp 213–222. https://doi.org/10.1007/978-3-319-07599-0_12

Brunner G (2021) CEIWR-HEC HEC-RAS River Analysis System: user's Manual Version 6.0. US Army Corps of Engineers Institute for Water Resources. HEC, Davis, CA, USA. https://doi.org/10.3390/w14071076

Bures L, Roub R, Sychova P et al (2019) Comparison of bathymetric data sources used in hydraulic modelling of floods. J Flood Risk Manag 12:e12495. https://doi.org/10.1111/jfr3.12495

Carlson DF, Fürsterling A, Vesterled L et al (2019) An affordable and portable autonomous surface vehicle with obstacle avoidance for coastal ocean monitoring. HardwareX 5:e00059. https://doi.org/10.1016/j.ohx.2019.e00059

Charbeneau RJ, Holley ER (2001) Backwater effects of bridge piers in subcritical flow. Center for Transportation Research, Bureau of Engineering Research, Accessed August 5 2024

Chow VT (1959) Open-channel Hydraulics. McGraw-Hill, New York

Flener C, Lotsari E, Alho P, Käyhkö J (2012) Comparison of empirical and theoretical remote sensing based bathymetry models in river environments. River Res Appl 28(1):118–133. https://doi.org/10.1002/rra.1441

Flynn KM (2006) Estimating magnitude and frequency of floods using the PeakFQ program. US Geological Survey. Accessed 5 August 2024

Ghaderi A, Daneshfaraz R, Dasineh M (2019) Evaluation and prediction of the scour depth of bridge foundations with HEC-RAS numerical model and empirical equations (Case Study: Bridge of Simineh Rood Miandoab, Iran). Eng J 23(6):279–295. https://doi.org/10.4186/ej.2019.23.6.279

Jeannotte TL, Mahmood TH, Vandeberg GS et al (2020) Impacts of cold region hydroclimatic variability on phosphorus exports: insights from concentration-discharge relationship. J Hydrol 591:125312. https://doi.org/10.1080/10106049.2023.2209541

Khandelwal A, Castillo T, González-Pinzón R (2023) Development of the Navigator: a Lagrangian sensing system to characterize surface freshwater ecosystems. Water Res 245:120577. https://doi.org/10.1016/j.watres.2023.120577

Lim YH, Voeller DL (2009) Regional flood estimations in Red River using L-moment-based index-flood and bulletin 17B procedures. J Hydrol Eng 14(9):1002–1016. https://doi.org/10.1061/(ASCE)HE.1943-5584.0000102

Lindenschmidt KE, Sydor M, Carson R, Harrison R (2012) Ice jam modelling of the Lower Red River. J Water Resour Prot 4(1):1–11. https://doi.org/10.4236/jwarp.2012.41001

Mehta DJ, Yadav S (2020) Analysis of scour depth in the case of parallel bridges using HEC-RAS. Water Supply 20(8):3419–3432. https://doi.org/10.2166/ws.2020.255

Mueller DS, Wagner CR, Rehmel MS et al (2009) Measuring discharge with acoustic Doppler current profilers from a moving boat. US Department of the Interior, US Geological Survey, Reston, Virginia. https://doi.org/10.3133/tm3a22

Muste M, Yu K, Pratt T, Abraham D (2004) Practical aspects of ADCP data use for quantification of mean river flow characteristics; part II: fixed-vessel measurements. Flow Meas Instrum 15(1):17–28. https://doi.org/10.1016/j.flowmeasinst.2003.09.002

Namara WG, Damisse TA, Tufa FG (2022) Application of HEC-RAS and HEC-GeoRAS model for Flood Inundation Mapping, the case of Awash Bello Flood Plain, Upper Awash River Basin, Oromiya Regional State, Ethiopia. Model Earth Syst Environ 8(2):1449–1460. https://doi.org/10.1007/s40808-021-01166-9

Neal ML, Mahmood TH, Kaemingk MA et al (2023) Mechanism of Cold Region Lake responses to climatic wetting: insights from a physically-based hydrologic model. AGU23. https://doi.org/10.1029/2019WR026932

Nezaratian H, Hassanjabbar A, Wu P (2023) Estimation of maximum scour depth around bridge piers under ice-covered conditions using data-driven methods. Int J Sediment Res 38(2):191–202. https://doi.org/10.1016/j.ijsrc.2022.07.008

Noor M, Arshad H, Khan M et al (2020) Experimental and HEC-RAS modelling of bridge pier scouring. J Adv Res Fluid Mech Therm Sci 74(1):119–132. https://doi.org/10.37934/arfmts.74.1.119132

Pathan AI, Agnihotri P (2021) Application of new HEC-RAS version 5 for 1D hydrodynamic flood modeling with special reference through geospatial techniques: a case of River Purna at Navsari, Gujarat, India. Model Earth Syst Environ 7:1133–1144. https://doi.org/10.1007/s40808-020-00961-0

Pinos J, Timbe L, Timbe E (2019) Evaluation of 1D hydraulic models for the simulation of mountain fluvial floods: a case study of the Santa Bárbara River in Ecuador. Water Pract Technol 14(2):341–354. https://doi.org/10.2166/wpt.2019.018

Rannie W (2016) The 1997 flood event in the Red River basin: causes, assessment and damages. Can Water Resour J 41(1–2):45–55. https://doi.org/10.1080/07011784.2015.1004198

Richardson EV, Davis SR (2001) Evaluating scour at bridges. United States Federal Highway Administration Office of Bridge Technology

Salalila A (2021) Autonomous Real-Time Water Quality Monitoring System. Dissertation, Washington State University. https://doi.org/10.1109/IEEECONF38699.2020.9389374

Salavitabar S, Li SS, Lak B (2022) Mapping underwater bathymetry of a shallow river from satellite multispectral imagery. Geosciences 12(4):142. https://doi.org/10.3390/geosciences12040142

Sando SK, McCarthy PM (2018) Methods for peak-flow frequency analysis and reporting for streamgages in or near Montana based on data through water year 2015. US Geological Survey, Scientific Investigations Report 2018-5046. https://doi.org/10.3133/sir20185046, Accessed August 5 2024

Schlauderaff MB (2021) Past Flooding Events and a 400 + Year Ring-Width Chronology of Bur Oak along the Red River in North Dakota and Minnesota. Dissertation, North Dakota State University

Silvia C, Ikhsan M, Wirayuda A (2021) Analysis of scour depth around Bridge Piers with Round Nose shape by HEC-RAS 5.0. 7 Software. J Phys Conf Ser 2021:012151. https://doi.org/10.1088/1742-6596/1764/1/012151

SonTek (2012) RiverSurveyor S5/M9 system manual firmware version 3.00. SonTek/YSI, San Diego, California

St. George S, Zeleznik J, Avila J, Schlauderaff J M (2022) The need for paleoflood investigations on the American reach of the Red River of the North. Holocene 32(3):220–225. https://doi.org/10.1177/09596836211060542

U.S. Army Corps of Engineers (2019) Lower Red Basin Retention (LRBR) Study. St. Paul District, St. Paul, Minnesota

Veilleux AG, Cohn T, Flynn K et al (2014) Estimating magnitude and frequency of floods using the PeakFQ 7.0 program: US Geological Survey Fact Sheet 2013–3108. US Geological Survey Fact Sheet, Accessed 5 August 2024

Vermeulen B, Sassi M, Hoitink A (2014) Improved flow velocity estimates from moving-boat ADCP measurements. Water Resour Res 50(5):4186–4196. https://doi.org/10.1002/2013WR015152

Zheng X, Maidment DR, Tarboton DG et al (2018) GeoFlood: large-scale flood inundation mapping based on high-resolution terrain analysis. Water Resour Res 54(12):10013–010033. https://doi.org/10.1016%2Fj.mex.2021.101527

Authors and Affiliations

Vida Atashi[1] · Yeo Howe Lim[1] · Taufiq H. Mahmood[2]

✉ Vida Atashi
vida.atashi@und.edu

Yeo Howe Lim
yeo.lim@und.edu

Taufiq H. Mahmood
taufique.mahmood@und.edu

[1] Department of Civil Engineering, University of North Dakota, Grand Forks, ND 58202, USA

[2] Harold Hamm School of Geology and Geological Engineering, University of North Dakota, Grand Forks, ND, USA